Reassessment of the Raman CO$_2$ densimeter

H.M. Lamadrid [a,b,*], L.R. Moore [a], D. Moncada [c], J.D. Rimstidt [a], R.C. Burruss [d], R.J. Bodnar [a]

[a] Department of Geosciences, Virginia Tech, Blacksburg, VA 24061, USA
[b] Department of Earth Sciences, University of Toronto, Toronto, ON, M5S 3B1, Canada
[c] Department of Geology and Andean Geothermal Center of Excellence (CEGA), Universidad de Chile, Plaza Ercilla 803, Santiago, Chile
[d] U.S. Geological Survey, National Center, Reston, VA 20192, USA

ARTICLE INFO

ABSTRACT

Raman spectroscopy has proven to be an effective tool to confirm the presence and abundance of CO$_2$ in fluid and melt inclusions. The Raman method for quantifying CO$_2$ abundance is based on the observation that the distance between the two Raman bands comprising the Fermi diad varies systematically with CO$_2$ density. In recent years, several Raman densimeters have been developed by different research groups to determine the density of CO$_2$ in fluid and melt inclusions. The different densimeters that have been proposed predict different densities for the same Fermi diad splitting, leading to large differences in estimated CO$_2$ contents for inclusions, depending on which densimeter is used to interpret the Raman data. In this study, we examine potential causes for variations in the various densimeters and show that these differences are mainly the result of using different Raman instruments and settings, different collection parameters, and different analytical methods.

Twelve experiments were conducted to test the variability associated with changing instrumental and analytical conditions, as well as to understand the differences between the various densimeters, using three different Raman instruments, with different laser sources and dispersion gratings. In all of the experiments, the splitting of the Fermi diad of CO$_2$ and CO$_2$ density at pressures from the liquid-vapor curve (6.0 MPa to 0.06 MPa) at ambient temperature (~22 °C) was calibrated using a high-pressure optical cell. The results show a consistent behavior whereby all analytical configurations show parallel trends in terms of the variation in Fermi diad splitting as a function of CO$_2$ density. The slopes of the lines representing the variation in Fermi diad splitting as a function of CO$_2$ density, as well as low density (pressure) data from other densimeters (Kawakami et al., 2003; Yamamoto and Kagi, 2006; Song et al., 2009; Fall et al., 2011; Wang et al., 2011) are remarkably similar, with a variation of about ~10% and a standard deviation of 3%. The differences observed in all densimeters, including previously published densimeters and the 12 experiments from this study, are most likely a function of variations in instrumentation, laser excitation wavelength, gratings, and analytical protocols used during the experimental calibration of the splitting of the Fermi diad. Based on results of this study, we recommend against using any published densimeter to interpret Raman data collected using an instrument other than that on which the calibration is based, and suggest that researchers develop a calibration that is applicable and specific to their instrument and data collection protocol.

© 2016 Elsevier B.V. All rights reserved.

1. Introduction

Carbon dioxide (CO$_2$)-bearing fluids are common in many geological environments (Roedder, 1984), including volcanic fumaroles and continental geothermal systems (Chiodini et al., 1998; Giggenbach, 1988, 1996), hydrothermal vents at mid-ocean ridges (Charlou et al., 1998, 2002), in various ore-forming systems (Roedder, 1984; Bodnar, 1995; Bodnar et al., 2014; Hedenquist and Henley, 1985; Roedder and Bodnar, 1997), abbysal serpentinites (Kelley, 1996), low to high grade

metamorphic rocks (Hollister and Burruss, 1976; Newton et al., 1980; Touret, 1971, 1981, 2001; Yardley, 1997), and mantle rocks sampled by upper mantle xenoliths (Roedder, 1965, 1984, 1994). Additionally, CO$_2$ is a common component in melt inclusions trapped during volcanic, magmatic and high-grade metamorphic processes (Wallace, 2005; Métrich and Wallace, 2008; Kent, 2008; Bartoli et al., 2013). Fluid and melt inclusions are the most reliable tools available to characterize the physical and chemical properties of paleo-crustal and mantle fluids, physical conditions of magmas, and much of our understanding of the pressure, density, temperature and composition of crustal (and upper mantle) fluids and melts comes from studies of fluid and melt inclusions (Roedder, 1984; Roedder and Bodnar, 1997; Frezzotti et al., 1994; Lowenstern, 2001; Mormone et al., 2011; Di Genova, et al., 2014;

* Corresponding author at: Department of Earth Sciences, University of Toronto, Toronto, ON, M5S 3B1, Canada
E-mail address: hm.lamadrid@utoronto.ca (H.M. Lamadrid).

Bodnar et al., 2014; Yardley and Bodnar, 2014; Frezzotti and Ferrando, 2015). Moreover, CO_2 is the second most abundant volatile species in magmas (in some cases in mafic and ultramafic magmas can be the most abundant), and affects the transport properties (density and viscosity) of magmas (Lowenstern, 2001; Mormone et al., 2011; Di Genova, et al., 2014).

Numerous techniques are available to determine the presence and/or concentration of CO_2 in fluid and melt inclusions, and the choice of technique depends on several factors. Some fluid inclusions (FI) show three fluid phases when observed at room temperature (inclusions "A" and "B" in Fig. 1), consisting of liquid and vapor CO_2 and an aqueous (H_2O) phase that is saturated in CO_2. For such FI, petrographic observations confirm the presence of CO_2 and the relative amounts of CO_2 and H_2O can be determined either by analyzing the FI by Raman spectroscopy after heating it to the homogenization temperature and using the relationship between Raman peak areas and CO_2/H_2O ratio (Azbej et al., 2007) or from microthermometric data (Bakker and Diamond, 2000). Similarly, the CO_2 concentration can be estimated by measuring the homogenization temperature of the liquid and vapor CO_2 to determine the CO_2 density and then use the relative volume proportions of the CO_2 and H_2O phases to estimate the bulk composition using a mass balance approach (Bodnar, 1983). This technique works well if the FI are large enough to measure the CO_2 homogenization temperature precisely (such as FI "A" in Fig. 1). Unfortunately, for small FI (<5 μm) and/or those in which the CO_2 liquid and vapor homogenize to the vapor phase, it is difficult to estimate the CO_2 concentration with high precision (Rosso and Bodnar, 1995). If the CO_2 concentration and/or density in the FI are sufficiently low, the FI will contain only vapor CO_2 at room temperature (such as FI "C" in Fig. 1). For these FI, the presence of CO_2 is sometimes indicated by the formation of a clathrate phase that melts at temperatures >0 °C and/or by a "melting event" that is observed when the FI is cooled to low temperatures (<−100 °C) and then heated through the CO_2 triple point temperature (−56.6 °C). In melt inclusions (MI) that contain low density CO_2 (Esposito et al., 2016; Moore et al., 2015; Fig. 1, inclusion "D") such that liquid and vapor CO_2 are not present at room temperature and do not form during cooling of the MI, it is

also difficult to estimate concentrations and in some cases to determine the presence of CO_2.

Alternatively, Raman spectroscopy can be used to confirm the presence of CO_2, even when its presence is not obvious during petrographic and/or microthermometric analyses. Carbon dioxide has a characteristic Raman spectrum that contains several well-defined and relatively intense peaks, even at relatively low CO_2 densities (Fig. 1). As summarized in Rosso and Bodnar (1995), the linear CO_2 molecule has four modes of vibration: a symmetric stretching mode (v_1), an anti-symmetric stretching mode (v_3), and two bending modes (v_{2a} and v_{2b}) that have the same frequency and form a degenerate pair. According to Gordon and McCubbin (1966), the symmetric stretching mode occurs at 1332.87 cm^{-1} and this mode has nearly the same energy as the second excited state of an infrared active bending mode, v_2. Because these two bands have nearly the same energy and the same symmetry species, they perturb each other in the excited state by a process known as Fermi resonance (Fermi, 1931). Fermi resonance causes the excited admixed states to split into two strong CO_2 lines referred to as the Fermi diad, with nominal frequencies of 1388.2 cm^{-1} (v_+; Fig. 1) and 1285.4 cm^{-1} (v_-; Fig. 1).

Some of the earliest Raman studies of the carbon dioxide molecule showed that the distance between the two peaks of the Fermi diad (peak splitting or Δ) (Fig. 1) is density (or pressure) dependent (Wright and Wang, 1973, 1975). Over the last 20–30 years, several groups (Rosso and Bodnar, 1995; Kawakami et al., 2003; Yamamoto and Kagi, 2006; Song et al., 2009; Fall et al., 2011; Wang et al., 2011) have used this behavior to develop Raman densimeters that relate the splitting of the Raman Fermi diad to the density of CO_2, as summarized in Table 1 and Fig. 2A. The relationship between CO_2 density and the Fermi diad splitting has been applied to estimate the density of carbon dioxide in FI and MI from a variety of different geological settings (Yamamoto et al., 2002; Yamamoto and Kagi, 2006; Yamamoto et al., 2007; Esposito et al., 2011; Steele-MacInnis et al., 2011; Bartoli et al., 2013; Hartley et al., 2014; Moore et al., 2015). The densimeters are mathematical expressions that relate CO_2 density to the splitting of the Fermi diad (Δ, cm^{-1}). All of the densimeters show a similar trend
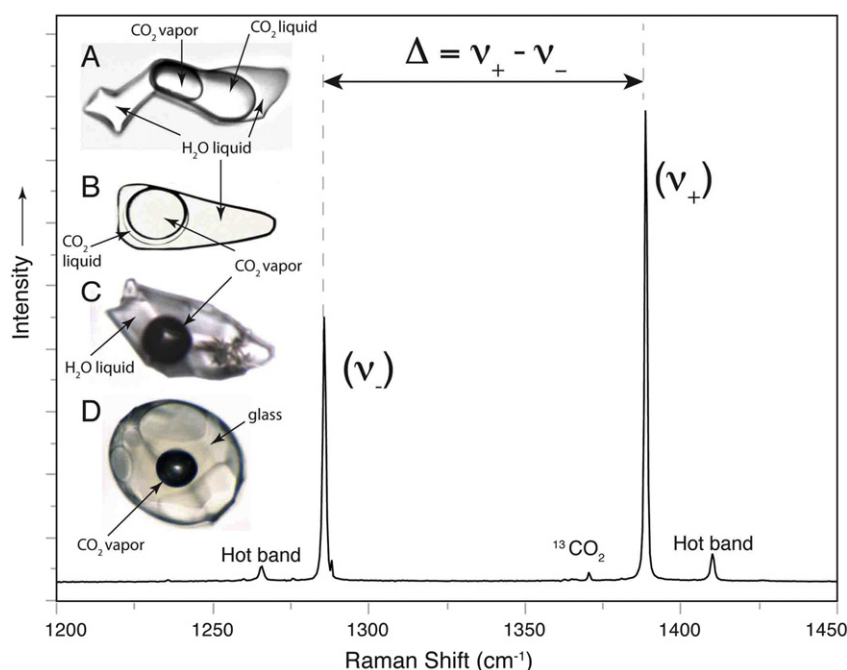
Fig. 1. Raman spectrum of CO_2 showing the Fermi diad and representative CO_2-bearing fluid and melt inclusions. The distance between v_+ and the v_- peaks of the Fermi diad is given by Δ (cm^{-1}) and is density (pressure) dependent. The low intensity hot bands shown are due to the thermal energy of the vibrating molecules and are not used in this study. (A) Three phase fluid inclusion containing liquid H_2O, and liquid and vapor CO_2. (B) Three phase fluid inclusion containing liquid H_2O, CO_2 vapor and a thin rim of liquid CO_2 surrounding the vapor bubble. (C) Fluid inclusion containing liquid H_2O and CO_2 vapor. (D) Melt inclusion containing glass and a CO_2 vapor bubble. All photos (A–D) taken at room temperature.

Table 1

Equations used to describe the relationship between density, pressure, and splitting of the Fermi diad for CO_2.

Source	Equation
Rosso and Bodnar (1995)	$\rho = 2.49\Delta + 102.68$
Kawakami et al. (2003)	$\rho = 0.03238697\Delta^3 + 10.08428\Delta^2 - 1046.189\Delta + 36{,}163.67$
Yamamoto and Kagi (2006)	$\rho = -0.01917(\Delta - 100)^3 + 0.1984(\Delta - 100)^2 - 0.241(\Delta - 100) - 0.341$
	$\rho = -0.00111808(\Delta - 100)^8 + 0.04498451(\Delta - 100)^7 - 0.7727143(\Delta - 100)^6 + 7.4128146(\Delta - 100)^5$
	$\quad - 43.468301(\Delta - 100)^4 + 159.54433(\Delta - 100)^3 - 357.7651(\Delta - 100)^2 + 448.2404\,(\Delta - 100) - 240.461$
Song et al. (2009)	$\rho = 0.74203\,(-0.019\Delta^3 + 5.90332\Delta^2 - 610.79472\Delta + 21{,}050.30165 - 3.54278$
Fall et al. (2011)	$\rho = -0.030314551\Delta^3 + 9.432834797\Delta^2 - 977.9384933\Delta + 33{,}780.38242$
Wang et al. (2011)	$\rho = 47{,}513.64243 - 1374.824414\Delta + 13.25586152\Delta^2 - 0.04258891551\Delta^3$
Lamadrid et al. (this study)	$P_{psi} = -176{,}807.6 + (1723.5547 \times \Delta) - 1722.7765 \times (\Delta - 102.866)^2$
	$\rho = -36.42055 + (0.354812 \times \Delta)$

ρ = density (g/cm^3) ; Δ = Fermi diad splitting (cm^{-1}); P_{psi} = Pressure (psi).

of increasing splitting of the Fermi diad, with increasing CO_2 density. However, the CO_2 density predicted from a measured splitting of the Fermi diad shows significant variation, depending on which densimeter is used (Fig. 2A). Moreover, because all of the densimeters are described by empirical polynomial equations, none can be extrapolated with confidence beyond the density region used to develop the empirical relationships, as shown in Fig. 2B.

If the density of CO_2 in FI or MI is relatively high $(\geq 0.21\ g/cm^3)$, such that both liquid and vapor CO_2 are present at room temperature or form during moderate cooling, the density of the CO_2 phase can be estimated with reasonable confidence using a combination of petrography and microthermometry. However, if the density of CO_2 in the FI or MI is low $(\leq 0.1–0.21\ g/cm^3)$, such as for FI from epithermal precious metal deposits (Bodnar et al., 1985), oceanic vents (Kelley, 1996) and most melt inclusions (Moore et al., 2015), these techniques cannot give a useful estimate of the CO_2 density. In addition, the inferred densities of CO_2 in FI and MI from these environments are lower than the lowest CO_2 densities used to develop most of the published densimeters. This requires an extrapolation of the densimeters beyond the range in which they are calibrated. Finally, relatively large relative differences (percent difference) in CO_2 densities are predicted by the various densimeters at low densities (Fig. 2C). The relative difference in density between the densimeter that predicts the highest density for a given Fermi diad peak splitting (Kawakami et al., 2003) and that which predicts the lowest density for the same Fermi diad peak splitting (Wang et al., 2011) remains reasonably constant at ~0.1 g/cm^3 over the range ~ 0 to ~1 g/cm^3 (Fig. 2). An uncertainty of $\pm 0.05\ g/cm^3$ represents a relatively small error if the density (pressure) is relatively high, but the relative error increases with decreasing density. For example, an uncertainty of $\pm 0.05\ g/cm^3$ for a CO_2 density of 0.9 g/cm^3 represents a relative error of ~11% (Fig. 3A). However, the same uncertainty of $\pm 0.05\ g/cm^3$ for a density of 0.1 g/cm^3 represents a relative error of ~100% (Fig. 3A). As will be discussed below, development of the CO_2 densimeter involves measuring the splitting of the Fermi diad at some known pressure. Thus, we can calculate the range (or uncertainty) in pressure corresponding to a $\pm 0.05\ g/cm^3$ range in density, and results of this calculation are shown on Fig. 3B. Accordingly, the pressure uncertainty associated with an uncertainty in density of $\pm 0.05\ g/cm^3$ for a nominal density of 1.0 g/cm^3 is ~29 MPa, and the pressure range associated with this same uncertainty in density for a nominal density of 0.1 g/cm^3 is ~4 MPa. As discussed below, a pressure error of 4 MPa is about 2 orders of magnitude greater than the error in pressure measurement during the calibration experiments. Thus, the differences between the various densimeters are not likely associated with uncertainties in pressure determination during measurement of the Fermi diad, and alternative factors which might influence these differences from one densimeter to the other should be explored.

It is clear from examination of the relationship between CO_2 density and the Fermi diad splitting shown in Fig. 2 that different laboratories report different relationships between these two parameters. Thus, a researcher will predict different CO_2 densities for the same measured

Fermi diad splitting, depending on which densimeter is used. For example, a measured splitting of the Fermi diad of 102.9 cm^{-1} corresponds to a CO_2 density of 0.17 g/cm^3 using the densimeter of Kawakami et al. (2003), whereas the Wang et al. (2011) densimeter predicts a density of 0.06 g/cm^3. These two density estimates would result in estimated CO_2 contents that differ by >100% for a given volume percent vapor in a MI.

Some researchers have proposed techniques to correct for instrument dependent calibrations to obtain a universal equation that is applicable in all laboratories (Lu et al., 2007). In this study, we re-examine the relationship between splitting of the Fermi diad and CO_2 density at low CO_2 pressures (densities), extending from the CO_2 liquid vapor curve at ~6.0 MPa (density = 0.211 g/cm^3) down to 0.06 MPa (density = 0.001 g/cm^3) at room temperature (~22 °C). This is the density (pressure) region in which it is difficult or impossible to determine the CO_2 density from petrographic or microthermometric analyses, and is also the region in which relative errors in density predicted by the various densimeters are largest. The results and fitted equations were compared to previously published experimental data (Kawakami et al., 2003; Yamamoto and Kagi, 2006; Song et al., 2009; Wang et al., 2011; Fall et al., 2011) to develop a densimeter for CO_2 that extends over the density range from 0.001 g/cm^3 to 0.205 g/cm^3. This density range corresponds to a pressure range from ~9 to 860 psi (0.0621 to 5.93 MPa) at ambient temperature (~22 °C), i.e., PT conditions in the CO_2 vapor field.

A review of the literature indicates that the methodologies followed to develop the various CO_2 densimeters are sound, yet different densimeters predict different densities for the same Fermi diad splitting (Fig. 2). Several previous studies of the pressure and temperature (density) dependence of Raman spectral features for volatile species (CO_2, CH_4) have acknowledged that their results follow similar, but offset trends (Song et al., 2009; Wang et al., 2011; Lu et al., 2007; Lin et al., 2007). These differences have been considered to be mostly the result of: 1) variations associated with instrumentation (hardware) (Lu et al., 2007; Wang et al., 2011), 2) variations in data collection, calibration, and interpretation procedures (Song et al., 2009), 3) variations in the experimental method and EOS used to interpret the data (Song et al., 2009; Lu et al., 2007). These possibilities led us to examine potential causes for variations in the different densimeters that have been reported in the literature by using assorted instrumental settings and collection parameters to analyze CO_2, and to test our calibration results with those developed using other Raman instruments and analytical methods. As such, several hundred Raman analyses of CO_2 were collected at various pressures and using different Raman instruments, excitation laser wavelengths and gratings.
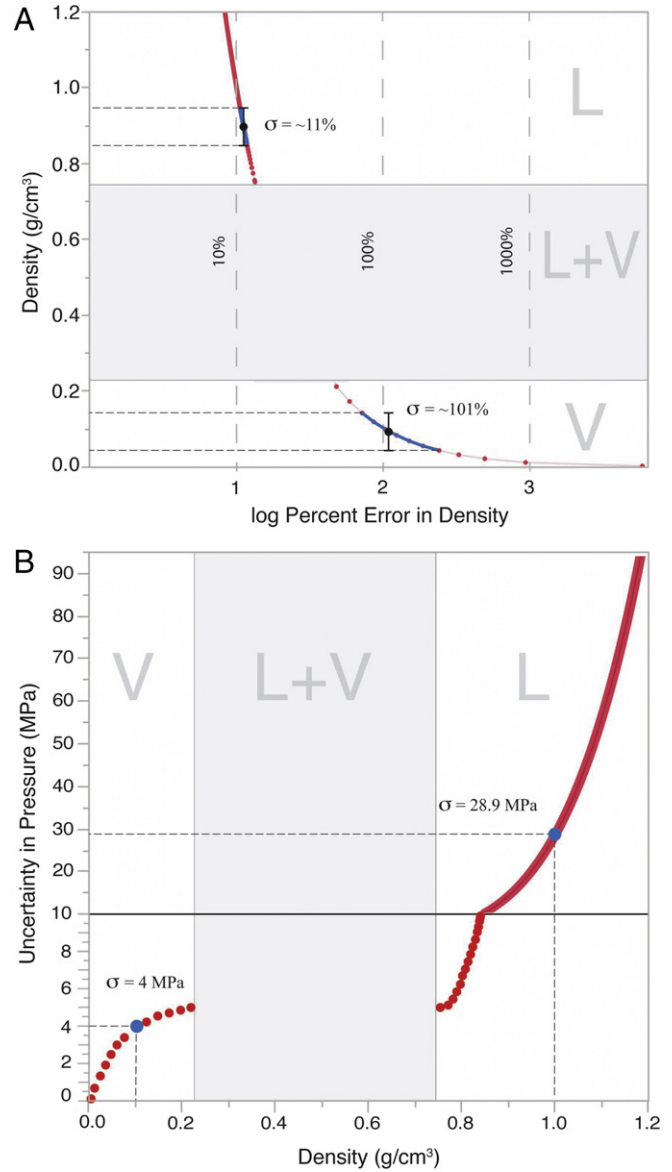
2. Analytical methods

The splitting of the Fermi diad in the Raman spectrum of CO_2 was calibrated as a function of pressure and temperature, using a high-pressure optical cell (HPOC) in the Vibrational Spectroscopy Laboratory in
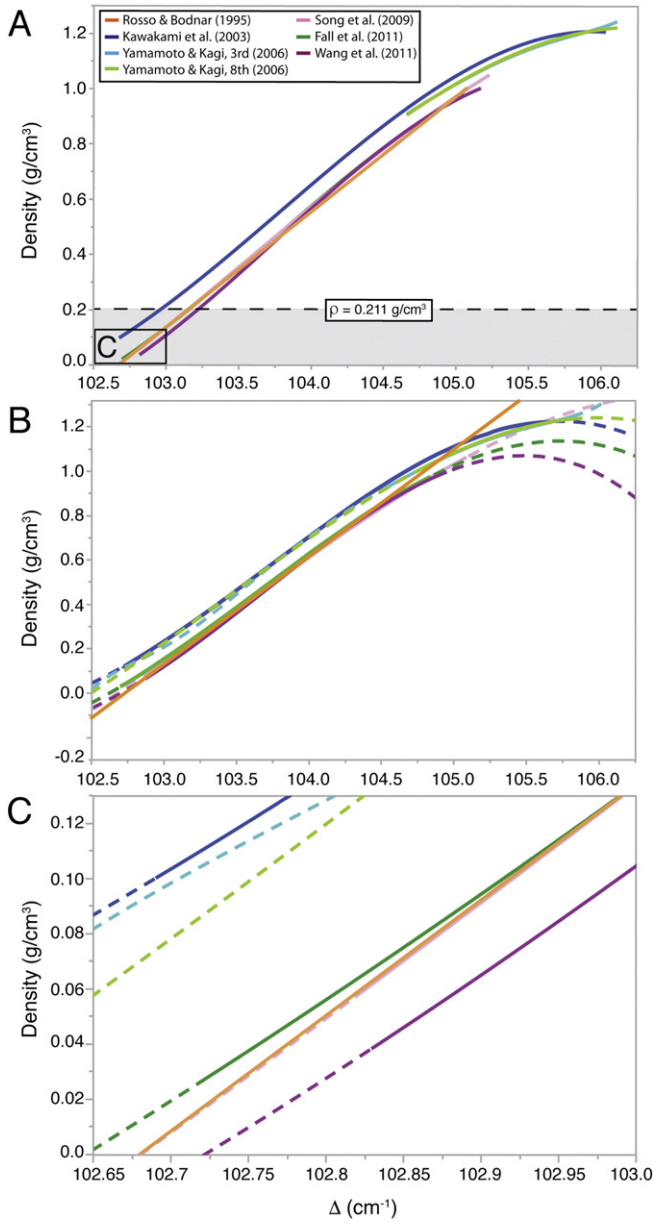
Fig. 2. Density of CO_2 as a function of the Fermi diad splitting predicted by various densimeters. (A) Density of CO_2 as a function of the Fermi diad splitting over the entire density range for which various densimeters have been calibrated. Densities <0.211 g/cm³ correspond to CO_2 vapor at ambient conditions (~22 °C) and are shown by the shaded region. (B) Densities predicted by the various published densimeters both within the density region in which calibration measurements were made (solid lines) and extrapolated to higher and/or lower densities using the published densimeter equations. (C) Enlargement of the low-density region shown in Fig. 2A. Tables 1 and 2 list the equations and the experimental conditions of the published densimeters, respectively.

Fig. 3. Comparison of the relative error in density corresponding to an absolute uncertainty in density of ±0.05 g/cm³, and the pressure uncertainty associated with a ±0.05 g/cm³ variation in density. (A) The relative error is density, shown as the log of the percent error (x-axis) as a function of density. An uncertainty of ±0.05 g/cm³ at a density of 0.9 g/cm³ represents a relative error, σ, of ~11%. The same uncertainty of ±0.05 g/cm³ at a density of 0.1 g/cm³ represents relative error of ~101%. The percent error increases logarithmically with decreasing density. (B) Uncertainty (or range) in pressure (MPa) required to produce an uncertainty of ±0.05 g/cm³ in density. The pressure uncertainty required to produce an uncertainty of ±0.05 g/cm³ in density for a density of 1.0 g/cm³ is 28.9 MPa, and for a density of 0.1 g/cm³ the pressure uncertainty is 4 MPa. For comparison the uncertainty in pressure determination in this study is ~0.03 MPa (or ~4 psi).

the Department of Geosciences at Virginia Tech (Fig. 4). The experimental setup is similar to the one used in previous studies (Lin et al., 2007; Fall et al., 2011). Kawakami et al. (2003) and Yamamoto and Kagi (2006) describe a similar experimental technique using an HPOC to develop the calibration curve for splitting of the Fermi diad as a function of CO_2 density, which was then used to determine the densities of CO_2-rich fluid inclusions in mantle xenoliths. Song et al. (2009) determined the relationship between peak splitting and density for densities along the CO_2 liquid-vapor curve by analyzing CO_2 contained in fused silica capillary capsules (FSCC). Wang et al. (2011) used both an HPOC and FSCC to determine the relationship between peak splitting and density. Details

of the experimental conditions used in these earlier studies are described in Table 2.

In this study, the optical cell (Fig. 4C, H) was connected to a manual screw press-type pressure generator (High-Pressure Equipment Model #50- 6-15; Fig. 4F). Pressure was monitored using two independent pressure transducers that were both connected to the HPOC and could be read simultaneously during the analyses. One was a Precise Instruments pressure transducer (Model 645) accurate to ±0.1% of the pressure output (pressure displayed in bars; Fig. 4B). The uncertainty in pressure for this transducer at the highest experimental pressure of 6.0 MPa (60 bars) was ±0.6 MPa (6 bars), and at the lowest
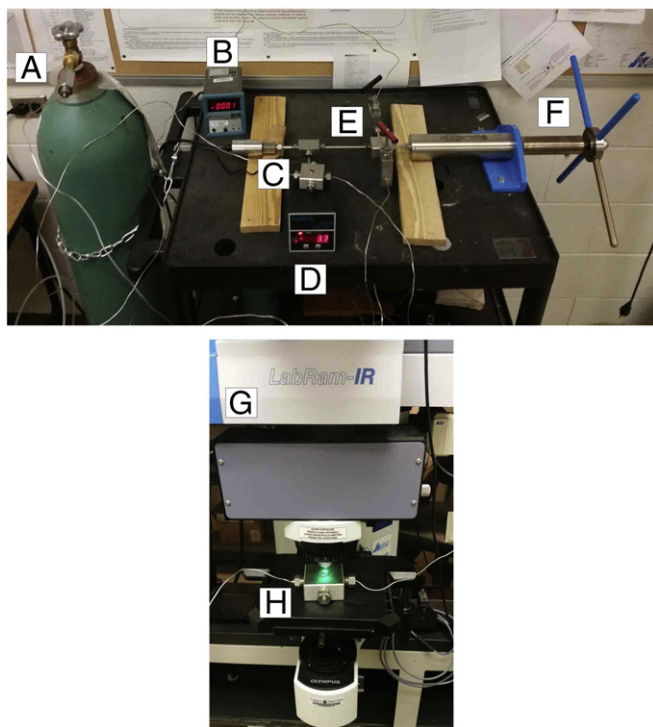
Fig. 4. The high-pressure optical cell (HPOC) used to determine the position of the Raman Fermi diad as a function of temperature and pressure. (A) CO_2 tank (99.999% pure). (B) Pressure transducer with digital output in bars. (C) Optical pressure cell. (D) Pressure transducer with digital output in psi. (E) Input and output valves. (F) Manual screw press-type pressure generator. (G) Optical microscope of the JY Horiba LabRam HR spectrometer. (H) Optical pressure cell during Raman analysis. Readers are referred to Lin et al. (2007) and Fall et al. (2011) for a more detailed description of the experimental setup.

experimental pressure of 0.1 MPa (1 bar) the uncertainty was ± 0.01 MPa (0.1 bars). The second transducer was a Setra pressure transducer (Model 204C) accurate to ± 0.25% of the pressure output (pressure displayed in psi) coupled with a Datum 2000 meter (Fig. 4D). The uncertainty for this transducer at the highest pressure of 870 psi (6.0 MPa) was ± 2.2 psi (0.01 MPa), and at the lowest pressure of 9 psi (0.06 MPa) the uncertainty was ± 0.02 psi (0.0001 MPa).

Commercially supplied ultra-high purity CO_2 (99.999% pure) (Fig. 4A) was used for the calibration experiments. The capillary system and HPOC were purged several times before each experiment to remove any other gases and/or water from the cell (Fig. 4C, H). The positions of the Fermi diad peaks were measured both along a decreasing pressure

path from the CO_2 liquid-vapor curve (6.1 MPa at 22 °C) to 0.06 MPa in 0.2 MPa increments, and along an increasing pressure path from 0.06 to 6.1 MPa in 0.2 MPa increments. All spectra were collected at ambient temperature (~22 °C), and the temperature of the pressure cell during each measurement was recorded by an Omega type-E thermocouple, calibrated against the freezing point of H_2O at 0 °C, that was inserted into a small hole drilled into the top of the pressure cell, 10 mm deep and 5 mm laterally from the gas chamber. The accuracy of temperature measurements was estimated to be ± 0.05 °C (Fall et al., 2011). Because the temperature in the cell sometimes changed by a few tenths of a degree Celsius owing to compression or expansion of the gas after the pressure was changed, the system was allowed to thermally equilibrate to ambient temperature (as shown by a constant readout from the temperature indicator) before the Raman spectrum was collected – this usually took ~5 min.

For the initial calibration experiments, Raman analyses were performed using a JY Horiba LabRam HR (800 mm) spectrometer (Fig. 4G), with 1800 grooves/mm gratings. The slit width was set to 150 μm, and the confocal aperture at 400 μm. Excitation was provided by a 514 nm (green) Laser Physics 100S-514 Ar + laser. The laser output was 50 mW at the source and ~10 mW at the sample. The laser was focused through a 3.5× objective (N.A. = 0.10) with a working distance of ~12 mm for the pressure cell. The laser spot size for the 3.5× objective is ~4 μm (Lin et al., 2007). The detector used is an electronically cooled open electrode 1024 × 512 pixel CCD. The mean value of three collections of 45 s each was taken to determine the Raman peak positions at each pressure. At pressures <1 MPa the collection times were increased by 30 s for every 0.2 MPa decrease in pressure to maintain good peak intensities (relative to background) to provide better fits during data analysis. The longest collection time was 300 s at 0.06 MPa.

In previous studies it was suggested that the absolute value of the difference in peak position (splitting) of the Fermi diad (Δ value) is sufficiently small to not be affected by the nonlinearity of the monochromer (McCreery, 2000). Nonetheless, in order to eliminate or minimize any potential contributions to uncertainty related to reproducibility and the linearity, the following precautions were taken:

1) Small variations in the Fermi diad splitting, ranging from 0.03 to 0.06 cm^{-1}, were observed for analyses conducted at different times but at the same P-T conditions, and we tested whether this variation was associated with the non-linearity of the spectrometer. In the instrument and software used for the calibration (JY Horiba LabRam HR800 and Labspec 5), the linearity is defined by the zero position (laser line) and the *Koeff* value. Note that other Raman systems and software might have different approaches to correct for nonlinearity. In the system used here, the *Koeff* value is calculated using the position of some other well-known Raman line. The small variations in Fermi diad peak splitting described above were

Table 2
Experimental conditions reported for the published densimeters.

Source	Experiment method	Pressure (MPa)	Density (g/cm³)	T (°C)	Reported error	Raman calibration method	Peak fitting function	EOS
Rosso and Bodnar (1995)	Gas cell SFI	0.5–50	0.1–1.21	RT	0.02 g/cm³	Ne light	Gaussian/Lorentz	Duschek et al. (1990) Bottinga and Richet (1981)
Kawakami et al. (2003)	HPOC	4–145	–	16.1–18.3 57.4–58.4 (SC)	0.1 cm^{-1}	Naphtalene	Lorentz	Sterner and Pitzer (1994)
Yamamoto and Kagi (2006)	HPOC	–	0.91–1.24		0.03 cm^{-1}	Naphtalene	Lorentz	Sterner and Pitzer (1994)
Song et al. (2009)	FSCC	–	0.06–1.05	22.1–23.5	0.1 cm^{-1}	Diamond	Not specified	Span and Wagner (1996)
Fall et al. (2011)	HPOC	1–30	–	− 10 to 22 35 (SC)	0.035 cm^{-1}	Silicon	Gaussian/Lorentz	Span and Wagner (1996)
Wang et al. (2011)	HPOC FSCC	2.2–35.7	0.04	RT 40 (SC)	0.054 cm^{-1}	Benzonitrile diamond	Gaussian	Span and Wagner (1996)
This study	HPOC	0.06–6.1	–	RT	0.0037 g/cm³ 0.01 cm^{-1}	Ne light	Gaussian	Span and Wagner (1996)

SFI: synthetic fluid inclusions, HPOC: high pressure optical cell, FSCC: fused silica capillary capsules, RT: room temperature, SC: supercritical temperatures.

observed when the *Koeff* value or linearity was defined using the laser (Rayleigh) line (Zero value) and the position of the silicon peak (520.5 cm^{-1}, *Koeff* value). These variations in peak splitting (0.03 to 0.06 cm^{-1}) correspond to uncertainties in density at our experimental conditions of ~0.03 g/cm^3. We note that when the positions of lines (such as the laser line and the silicon peak) are used to set the value of *Koeff* to define the linearity, the linearity is only defined in the spectral region between the two lines used to establish the linearity. As such, Lin et al. (2007) found that selecting a Raman line (band) closer to the spectral region of interest as the *Koeff* value minimizes uncertainties generated by this random error. We, therefore, defined the linearity of the spectrometer (*Koeff* value) in the spectral region of interest using the laser (Rayleigh) line and the Ne line at 1458.58 cm^{-1}. Additionally, to better compensate for the nonlinearity of the monochromator, two Ne emission lines (1031.42 cm^{-1} and 1458.58 cm^{-1}) were recorded *simultaneously* with the CO$_2$ bands using a Ne lamp that is permanently fixed into the optical path of the Raman system. It is important to note that the positions of the Ne lines in our study are relative to the laser line at 514.532 nm. If a different excitation laser wavelength is used, the appropriate Ne (or other source) lines corresponding to that excitation wavelength must be used for calibration and to bracket the Fermi diad. Using the measured splitting of the CO$_2$ Fermi diad (Δ and the measured and real, or known, (427.16 cm^{-1}) distances between the Ne lines, the corrected splitting (real) of the CO$_2$ Fermi diad was determined according to the following expression:

$$\Delta_{CO_2}^{Corrected} = \left(\frac{\Delta_{Ne}^{Known}}{\Delta_{Ne}^{Measured}} \right) \Delta_{CO_2}^{Measured} \qquad (1)$$

where $\Delta_{CO_2}^{Corrected}$ is the corrected splitting of the Fermi diad, Δ_{Ne}^{Known} and $\Delta_{Ne}^{Measured}$ are the known and measured separation between the 1458.58 cm^{-1} and 1031.42 cm^{-1} Ne emission lines, respectively, and $\Delta_{CO_2}^{Measured}$ is the measured splitting of the CO$_2$ Fermi diad peaks (v_+ and v_-, cm^{-1}) in the Raman spectrum. The correction assumes that the difference between the known (1458.58 cm^{-1} and 1031.42 cm^{-1}) and measured positions for the Ne lines is proportional to the difference between the real and measured peaks of the Fermi diad at ~1388.2 cm^{-1} and ~1285.4 cm^{-1} (Fig. 1).

2) Different Raman systems offer different methodologies for identifying the spectral region of interest and for collecting and compiling the spectral data. With the Raman system used in this study (JY Horiba LabRam HR), the region of interest over which the Raman spectrum is collected, i.e., the spectral region that includes the Fermi diad and the Ne reference lines, can be defined using different methods. The spectral window that is sampled and recorded simultaneously by the detector varies as a function of the gratings used in the spectrometer (the system used in this study has the option of using 600, 1800 or 2400 grooves/mm gratings). Thus, in some cases it may not be possible to record spectra over the entire range of interest in one window (single window collection), and several collection windows or spectral ranges must be defined and collected and then stitched together to obtain the entire spectrum. With the JY system, this method is referred to as an "extended range" collection (Labspec 5) or "multiwindow" collection (Labspec 6). The multi-window/extended window collection is an automatic function of Labspec Software that allows a spectrum to be acquired over an extended range by taking a number of individual windows and 'stitching' these together. In this study, differences in the measured Fermi diad peak splitting of 0.4 to 0.6 cm^{-1} were observed for a given P-T (density) condition when an extended window collection method was used rather than a single window collection. That is, the

reproducibility was poorer if the different Raman lines were collected in different windows and at different times and the windows were then stitched together to produce the entire spectrum, compared to collecting all lines of interest simultaneously in a single window. These differences in splitting of the Fermi diad at the P-T conditions of the analyses represent uncertainties in the density of ~0.1 to 0.2 g/cm^3. To eliminate this contribution to uncertainty and to enhance the reproducibility in the measured Fermi diad splitting for a given pressure (density), single window collections were used after centering the spectrometer at a position (1250 cm^{-1}) such that the CO$_2$ Fermi diad and the two Ne bracketing lines could be collected simultaneously in the same spectral window using the 1800 grooves/mm grating.

In order to further test the reproducibility of the analytical method described above and to test for instrumental variations, densimeters were developed using the HPOC on other Raman systems and on the same Raman instrument but with different laser excitation sources and/or gratings. In addition to the 514 nm laser described above, the JY Horiba LabRam HR (800 mm) Raman instrument at Virginia Tech is also equipped with a 632.9 nm He-Ne laser with a power of 20 mW at the source and ~2 mW at the sample, with 600, 1800 and 2400 grooves/mm gratings that can be used with both lasers. At the U. S. Geological Survey in Reston, VA the splitting of the Fermi diad was measured at different pressures (CO$_2$ densities) using a JY Horiba LabRam HR (800 mm) Raman system equipped with a 532.06 nm (frequency doubled Nd: YAG laser, 532.06 nm, ~20 mW output), a 5× objective, and 600 and 1800 grooves/mm gratings, with the confocal aperture set at 100 μm. During the analyses at the USGS, it was not possible to collect spectra for the Ne lines and the Fermi diad simultaneously. The instrument calibration at the USGS followed procedures similar to those of Wang et al. (2011), with zero correction using the laser (Rayleigh) line set at 0.0 nm and a *Koeff* correction using the silicon peak at 520.6 cm^{-1}. The relationship between CO$_2$ density and splitting of the Fermi diad was also measured on a JY Horiba Standard XploRA PLUS, equipped with 532 nm and 785 nm lasers and 600, 1800, and 2400 grooves/mm gratings. The spectral resolution varied from ~8 to 1.4 cm^{-1}, depending on the analytical settings. The slit width was set to 150 μm, and the confocal aperture was set at 400 μm. This system has a 1024 × 256 pixel TE deep air-cooled (−60 °C) CCD. The same 3.5× objective (N.A. = 0.10) used for analyses at Virginia Tech was used for these measurements. The XploRA instrument uses a NIST traceable and patented "autocalibration" for all laser and grating combinations, and a manual calibration such as described above for the LabRam instruments was not possible.

The positions of all Raman lines collected using the different instrumental and analytical combinations described above were determined after baseline correction and Gaussian peak fitting using Labspec 5 software. Previous studies (Izraeli et al., 1999; Fukura et al., 2006; Lin et al., 2007) demonstrated that least-squares fitting applied to Raman spectra improves the precision by ~30 times compared to that estimated based on the detector pixel resolution, and Lin et al. (2007) reported an uncertainty in peak position of ~0.02 cm^{-1} using the same LabRam HR800 instrument and analytical and calibration procedures as described here.

3. Results

A total of 183 Raman spectra were collected over the range from ~0.06 to 6.0 MPa at room temperature (~22 °C) to determine the relationship between CO$_2$ pressure (density) and the distance between the peaks of the Fermi diad of CO$_2$ (Electronic Annex A). We note that although all published Raman CO$_2$ densimeters relate the splitting of the Fermi diad to CO$_2$ density, all of the densimeters were obtained by measuring the splitting of the Fermi diad as a function of the CO$_2$ pressure rather than density. The pressure was then converted into CO$_2$
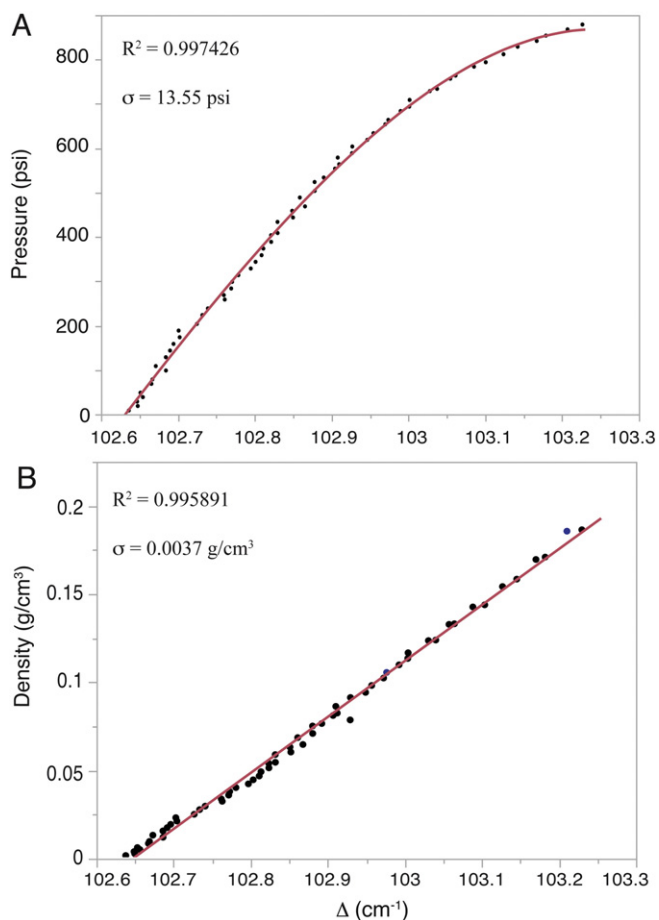
Table 3
Analytical conditions and calculated Fermi diad peak splitting, density and uncertainty in peak splitting.

Pressure (psi)	Pressure (MPa)	Temperature (°C)	Δ_{Real}[a]	Density[b] (g/cm^3)	Error Δ_{Real} (cm^{-1})
9	0.06	23	102.64	0.001	0.007
19	0.13	23	102.65	0.002	0.002
29	0.2	23	102.65	0.004	0.007
39	0.27	22.9	102.65	0.005	0.01
49	0.34	23.1	102.65	0.006	0.014
69	0.48	22.8	102.67	0.009	0.012
79	0.54	23.1	102.67	0.010	0.007
99	0.68	23	102.68	0.013	0.017
109	0.75	23.1	102.67	0.014	0.007
129	0.89	23	102.68	0.017	0.007
144	0.99	23	102.69	0.019	0.005
159	1.1	22.9	102.69	0.021	0.007
174	1.2	23	102.70	0.023	0.003
189	1.3	22.8	102.70	0.025	0.005
204	1.41	23	102.73	0.027	0.017
224	1.54	22.8	102.73	0.030	0.012
239	1.65	23	102.74	0.032	0.005
259	1.79	22.6	102.76	0.035	0.005
269	1.85	23	102.76	0.037	0.02
284	1.96	22.6	102.77	0.039	0.005
299	2.06	23	102.77	0.042	0.002
314	2.16	22.6	102.78	0.044	0.017
329	2.27	23.1	102.80	0.046	0.01
344	2.37	22.6	102.80	0.049	0.007
359	2.48	23.2	102.81	0.051	0.015
374	2.58	22.5	102.81	0.054	0.017
389	2.68	23.2	102.82	0.057	0.007
404	2.79	22.4	102.82	0.059	0.012
409	2.82	23.1	102.83	0.060	0.012
434	2.99	22.4	102.83	0.065	0.017
444	3.06	23.1	102.85	0.067	0.0071
459	3.16	22.3	102.85	0.070	0.005
469	3.23	23.1	102.87	0.071	0.002
489	3.37	22.2	102.86	0.076	0.002
504	3.47	23.1	102.88	0.078	0.01
524	3.61	22.1	102.88	0.083	0.015
534	3.68	23.1	102.89	0.085	0.01
554	3.82	22.6	102.90	0.090	0.015
564	3.89	23.1	102.91	0.091	0.002
579	3.99	22.5	102.91	0.095	0.012
589	4.06	23.1	102.93	0.087	0
604	4.16	22.5	102.93	0.101	0.014
619	4.27	23.2	102.95	0.104	0.008
634	4.37	22.4	102.95	0.109	0.008
654	4.51	23.1	102.97	0.113	0.007
664	4.58	22.4	102.97	0.117	0.002
684	4.72	23.1	102.99	0.122	0.012
694	4.78	22.3	103.00	0.126	0.005
709	4.89	22.3	103.00	0.129	0.015
729	5.01	22.2	103.03	0.137	0.01
734	5.06	23.3	103.04	0.137	0.017
757	5.22	22.3	103.05	0.147	0
764	5.27	23.3	103.06	0.148	0.005
784	5.41	22.2	103.09	0.158	0.01
794	5.47	23.3	103.10	0.160	0.01
812	5.6	22.3	103.12	0.171	0.007
829	5.72	23.3	103.14	0.176	0.01
842	5.81	22.2	103.17	0.188	0.022
854	5.89	23.3	103.18	0.190	0.012
868	5.98	22.3	103.21	0.206	0.02
879	6.06	23.3	103.23	0.207	0.014

[a] Fermi diad splitting obtained by using Eq. (1).
[b] Densities calculated using Span and Wagner (1996) EOS.

Fig. 5. Pressure (A) and density (B) of CO_2 as a function of the splitting of the Fermi diad (distance between ν_+ and the ν_- peaks of the Fermi diad) for CO_2 measured with the HPOC in this study. Data are listed as Electronic Appendix A.
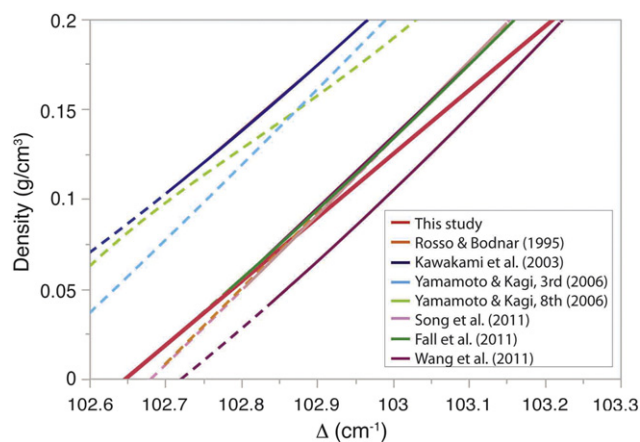
the two Ne lines (1031.42 cm^{-1} and 1458.58 cm^{-1}) used in our calibration was on average $\pm$ 0.02 cm^{-1}, with a standard deviation of 0.015 cm^{-1}. The corrected values of the Fermi diad splitting ($\Delta_{CO_2}^{Corrected}$) obtained from Eq. (1) for the three different collections vary by $\pm$ 0.009 cm^{-1}, with a standard deviation of 0.005 cm^{-1}. The average of the three Fermi diad peak splitting collections, $\Delta_{CO_2}^{Corrected}$, as well as experimental pressures, temperatures, densities and errors are shown in Table 3. The pressure (psi) at which the Raman spectrum was collected was fitted as a function of the corrected splitting of the Raman Fermi diad (Δ_{Real}) (Fig. 5a) using a 2nd order polynomial according to:

$$P_{psi} = -176807.6(1220.90) \\ + 1723.55(11.88)\Delta_{CO_2}^{Corrected} - 1722.77(65.55)\left(\Delta_{CO_2}^{Corrected} - 102.866\right)^2 \tag{2}$$

where $\Delta_{CO_2}^{Corrected}$ is the corrected splitting of the Fermi diad in cm^{-1} and P_{psi} is pressure in psi. The standard deviation was calculated from the residual plot $1\sigma = 13.55$ psi, and this error in pressure corresponds to an uncertainty of 0.008 cm^{-1} in the Fermi diad splitting, with a R^2 of 0.997426. The standard error for each term is shown in parentheses.

We note that the relationship between Fermi diad splitting and pressure described by Eq. (2) is based on measurements obtained at ambient temperature ($\sim$22 $\pm$ 1 °C). Thus, Eq. (2) should only be used when analyzing CO_2 at room temperature, and for pressures (and densities) in the CO_2 vapor field.

In the present study, the density corresponding to the temperature and pressure condition of every analysis was calculated using the Span and Wagner (1996) EOS as implemented in the NIST

density using an equation of state (EOS), as described further below. The pressure range in our experiments extends from the CO_2 liquid-vapor curve ($\sim$6.0 MPa at $\sim$22 °C) to the lowest pressure (0.06 MPa) at which the CO_2 peaks could be resolved during three consecutive collections. The difference in peak splitting of the three measurements at each pressure was generally less than $\pm$0.02 cm^{-1}, with a standard deviation of 0.006 cm^{-1}. The difference in the measured distance between

Fig. 6. Comparison of published CO_2 densimeters with the densimeter developed in this study. Note that all of the densimeters have been extrapolated by various amounts beyond the range in which they were calibrated, as shown by the dashed lines. The densimeter developed in this study was calibrated over the density range from 0.001 g/cm³ to 0.211 g/cm³, corresponding to a pressure range from 0.06 to 6.0 MPa. Data are listed in Table 3.

online calculator (http://webbook.nist.gov/chemistry/fluid/) for thermophysical properties of fluids. Thus, as noted above, because all studies that have developed the CO_2 densimeter measured the pressure and converted this value to a density using an EOS, some variation between densimeters might be related to the choice of EOS used to convert the pressure to density (see Table 2 for a listing of the EOS used in previous studies). We note, however, that over the P-T range of this study, differences in the volumetric (Pressure-Volume-Temperature, or PVT) properties for CO_2 predicted by the various EOS are negligible, and the NIST calculator was used due to its flexibility and ease of use. Thus, differences in various densimeters shown in Fig. 2 are not the result of using different EOS to interpret the PVT data for CO_2. After converting the experimental pressures (and temperatures) to density using the Span and Wagner (1996) EOS, CO_2 density was fitted as a function of the corrected splitting of the Fermi diad ($\Delta_{CO_2}^{Corrected}$) according to (Fig. 5B):

$$\rho = -36.42(0.31) + 0.355(0.01)\Delta_{CO_2}^{Corrected} \tag{3}$$

where ρ is density in g/cm³ and $\Delta_{CO_2}^{Corrected}$ is the Fermi diad splitting in cm^{-1}. The standard deviation of the differences between the actual and predicted values determined from the residual plot is 0.0037 g/cm³, corresponding to an error of ~0.01 cm^{-1} in the Fermi diad splitting, and the $R^2 = 0.995891$. The standard error for each term is shown in parentheses. The densities predicted by Eq. (3) were compared to other published Raman densimeters (Fig. 6). Our revised densimeter predicts CO_2 densities that are in general agreement with results from Fall et al. (2011), Song et al. (2009), Wang et al. (2011), and Rosso and Bodnar (1995). At a given pressure and temperature, densities predicted by the Kawakami et al. (2003) and Yamamoto and Kagi (2006) densimeters are significantly higher than those predicted by our model, although we note that we have extrapolated those densimeters (especially those of Yamamoto and Kagi, 2006) well beyond the density range over which they have been calibrated. While the various densimeters predict different densities for the same measured Fermi diad splitting, the trends for all densimeters are parallel to each other and to the trend predicted by Eq. (3) (this study).

3.1. Variability associated with instrumental configuration and analytical conditions

Raman spectra of CO_2 were collected over a range of pressures extending from the pressure on the CO_2 liquid-vapor curve (~6.0 MPa or 838 psi) at ambient temperature (~22 °C) to the lowest pressure at which the CO_2 Fermi diad bands could be measured (~0.06 MPa or 9 psi), to determine the relationship between CO_2 density and the splitting of the Fermi diad for 12 different Raman analytical configurations. Six of the experiments were conducted at Virginia Tech using the 514 nm and 632 nm lasers with the 600, 1800 and 2400 grooves/mm gratings; two experiments were conducted at the USGS in Reston, VA using a JY Horiba LabRam Raman system, a 532 nm laser and 600 and 1800 grooves/mm gratings, and three experiments were conducted using the JY Horiba Standard XploRA Plus Raman system equipped with a 532 nm laser and 1800 and 2400 grooves/mm gratings, and with a 785 nm laser with 1800 grooves/mm grating. For all analyses, the CO_2 density corresponding to the pressure (and temperature) at which the Fermi diad was measured was calculated using the Span and Wagner (1996) EOS as previously described. All results, including the data from the published densimeters, (Kawakami et al., 2003; Yamamoto and Kagi, 2006; Song et al., 2009; Fall et al., 2011; Wang et al., 2011) are tabulated in Table 4, Electronic Annex B and Fig. 7.

Table 4
Raman instruments and configurations, densimeters, slopes of fitted lines, and fitting statistics.

Experiment	Raman instrument	Laser (nm)	Gratings	Fitted equation	Residual error[b] (g/cm³)	Slope (g/cm³/cm⁻¹)	R^2
Eq. (3) Ne lines	JY Horiba Labram 800	514	1800	$\rho = -36.42(0.31)^a + 0.355(0.003)\Delta$	0.002	0.355	0.996
VT 514 nm 600 g	JY Horiba Labram 800	514	600	$\rho = -35.679(1.302) + 0.347(0.013)\Delta$	0.004	0.347	0.986
VT 514 nm 1800 g	JY Horiba Labram 800	514	1800	$\rho = -36.635(0.293) + 0.357(0.003)\Delta$	0.004	0.357	0.999
VT 514 nm 2400 g	JY Horiba Labram 800	514	2400	$\rho = -38.025(0.305) + 0.371(0.003)\Delta$	0.002	0.371	0.999
VT 632 nm 600 g	JY Horiba Labram 800	632	600	$\rho = -37.8(2.4) + 0.368(0.023)\Delta$	0.005	0.368	0.965
VT 632 nm 1800 g	JY Horiba Labram 800	632	1800	$\rho = -35.424(0.86) + 0.345(0.008)\Delta$	0.003	0.345	0.992
VT 632 nm 2400 g	JY Horiba Labram 800	632	2400	$\rho = -40.377(0.829) + 0.394(0.008)\Delta$	0.002	0.394	0.995
USGS 532 nm 600 g	JY Horiba Labram 800	532	600	$\rho = -37.387(1.027) + 0.364(0.009)\Delta$	0.005	0.364	0.988
USGS532nm 1800 g	JY Horiba Labram 800	532	1800	$\rho = -37.371(0.224) + 0.364(0.002)\Delta$	0.001	0.364	0.999
XplorA 532 nm 1800 g	XploRA Plus	532.	1800	$\rho = -38.891(0.874) + 0.379(0.008)\Delta$	0.002	0.379	0.994
XplorA 532 nm 2400 g	XploRA Plus	532	2400	$\rho = -39.737(0.671) + 0.387(0.068)\Delta$	0.003	0.387	0.996
XplorA785nm 1800 g	XploRA Plus	785	1800	$\rho = -38.016(0.694) + 0.370(0.007)\Delta$	0.002	0.370	0.996
Kawakami et al. (2003)[c]	Chromex 250is	514	—	$\rho = -35.25(2.916) + 0.344(0.028)\Delta$	0.007	0.344	0.954
Song et al. (2009)	JY Horiba Labram 800	532	1800	$\rho = -39.548 + 0.385\Delta$	—	0.385	1[+]
Wang et al. (2011)[c]	JY Horiba Labram 800	532	1800	$\rho = -35.652(0.578) + 0.347(0.006)\Delta$	0.004	0.347	0.991
Fall et al. (2011)[c]	JY Horiba Labram 800	514	1800	$\rho = -39.441(0.164) + 0.384(0.002)\Delta$	0.001	0.384	0.999

nm = laser wavelength, σ = density, Δ = Fermi diad splitting (cm^{-1}).
[a] In parenthesis is the standard error for the intercept and for the slope.
[b] Error = standard deviation of the residuals (difference from the predicted density equation to the real data).
[c] Only data lower than 0.2 g/cm³, [+] only 2 data points.

4. Discussion

4.1. Variations associated with instrumentation (hardware)

The comparison tests using different Raman configurations identified relatively small but systematic variations in the relationship between Fermi diad splitting and density (Fig. 7A). While the density predicted for a given Fermi diad splitting for the different instrumental combinations varies, the trends in Fermi diad splitting versus density for the various combinations are essentially parallel to each other (Fig. 7A), and over the range of conditions examined, the relationship of Fermi diad splitting to density is linear (Fig. 7B). The calculated slopes (m) for the different calibration lines vary from 0.3442 to 0.3935 which represents a ~ 12% relative difference between all the slopes. The average slope is 0.3663 with a standard error from the mean of 0.0041 (1.01%). This parallel behavior is similar to the trend observed for the extrapolated densimeters (Figs. 2C and 6).

One factor often ignored in Raman studies is the ambient temperature conditions in the laboratory and its effect on spectrometer

Fig. 7. Comparison of the different CO_2 densimeters developed in this study. (A) Data for the splitting of the Fermi diad, Δ, as a function of density for the different Raman analytical configurations. VT refers to analyses conducted at Virginia Tech using the JY Horiba LabRam HR system; USGS refers to analyses conducted at the U. S. Geological Survey using a JY Horiba LabRam HR system; XploRA refers to analyses conducted at Virginia Tech using a JY Horiba XploRA Raman system; 514 nm, 632 nm, 532 nm and 785 nm refer to the laser excitation wavelength, and 600, 1800, and 2400 refer to the number of grooves/mm of the grating used. The data set labeled VT 514 nm 1800 represents measurements without the Ne line correction. (B) Fitted lines corresponding to the different data sets shown in Fig. 7A. The dashed line is the relationship between Fermi diad peak splitting and density predicted by Eq. (3), that was developed using the data in Fig. 7A labeled "VT 514 nm 1800" after correcting the peak positions using the positions of the bracketing Ne lines collected simultaneously with the CO_2 spectrum.

performance and could explain some of the differences observed between published CO_2 densimeters (Gaufrès et al., 1995; Mestari et al., 1997; Fukura et al., 2006). Fukura et al. (2006) monitored changes in the fluorescence spectrum of ruby with time (the reader is referred to Fig. 5 in Fukura et al., 2006). Their results show that changes in ambient laboratory temperature of as little as 0.8 °C were responsible for variations in the peak position of ~0.1 cm^{-1}. Other workers had observed changes in peak position in the range of 0.1 to 0.3 cm^{-1} per degree Celsius of room temperature change (Gaufrès et al., 1995; Mestari et al., 1997). These variations suggest that as the room temperature changes, thermal expansion or contraction of spectrometer occurs (Fukura et al., 2006). In the Virginia Tech lab we recorded daily temperature fluctuations in the range ~ 1 °C during a normal operating day (~12 h). As such, temperature fluctuations while collecting the data cannot completely explain the differences recorded.
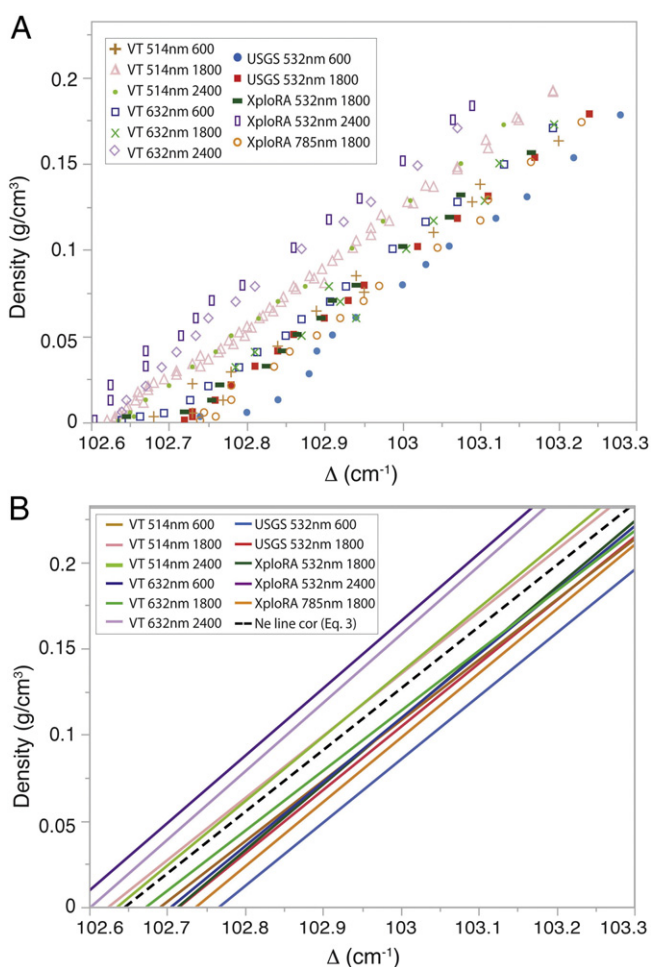
Another possible explanation that could account for the differences observed using different Raman configurations, as well as the differences observed in the published densimeters, is the manner in which light interacts with its environment as it travels between the laser source, the optics of the microscope, and the diffraction gratings to the detector. Minuscule differences in the construction of any part of the hardware can lead to some small but constant differences between the Raman configurations and could explain the differences observed in this study. For example, the diffraction gratings used in the Raman instruments involved in this study consist of a hard, optically flat surface etched with a large number of parallel and closely spaced grooves. A small difference in the etching of the gratings, or in the materials used for the gratings, can potentially change the angle in which light is dispersed. Moreover, changes in other instrumental parameters like the confocal aperture and the slit can potentially affect the spectral resolution depending on the Raman instrument, and could also generate small but systematic differences in the Raman peak position. These possibilities should be examined further, but this topic is beyond the scope of the present study.

4.2. Variations associated with data collection, calibration, interpretation, procedures and EOS.
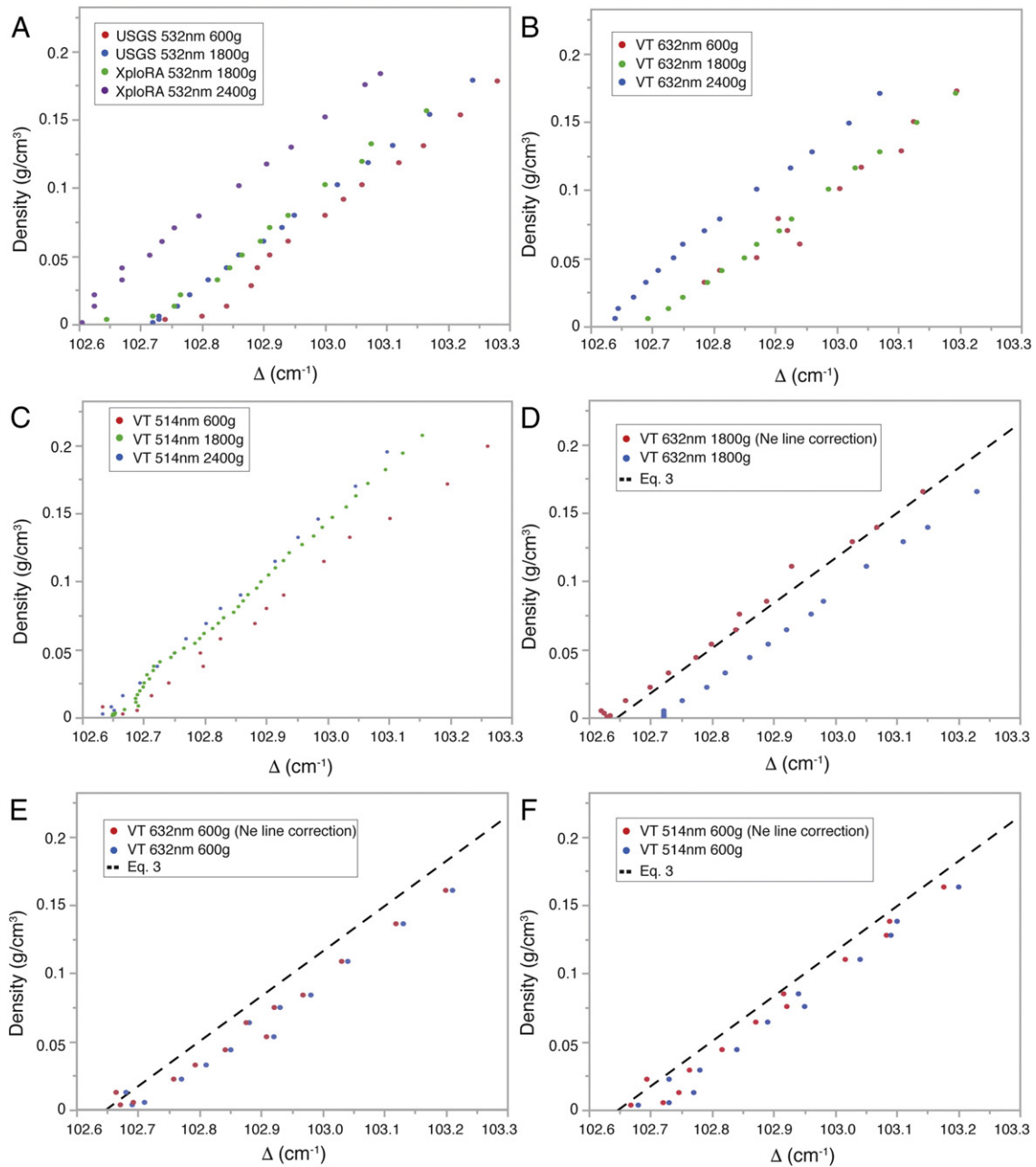
Our results show that the choice of grating has a relatively significant effect on the Raman spectrum. When using the same laser excitation wavelength with different gratings, we observed a correlation between different instruments and laser wavelengths (514, 532 and 632 nm. At the same CO_2 density, data collected with the 600 grooves/mm grating shows a greater splitting of the Fermi diad compared to measurements obtained with the 1800 and 2400 groove/mm gratings (Fig. 8A-B-C). In addition, using different Raman instruments but with similar excitation wavelength (532 nm) and gratings (1800 grooves/mm) produces similar peak splitting versus density relationships (Fig. 8A).

The effectiveness of using the known positions of Ne lines to correct peak positions was tested using four different Raman combinations, including the 514 and 632 nm lasers with the 600 and 1800 grove/mm gratings. Since the Raman shift depends on the laser wavelength, the Ne lines used with the 514 nm laser (1031.42 and 1458.58 cm^{-1}) were not at the same position as the lines obtained when the 632 nm laser is used (1371.28 and 1582.54 cm^{-1}). In all cases, using the Ne lines to correct the positions of the Fermi diad lines and, therefore, the splitting of the Fermi diad, shifts the data points closer to values predicted by Eq. (3) (Fig. 8D-E-F). However, the 600 grooves/mm gratings produce a lower spectral resolution and can produce larger errors associated with fitting the less intense peaks at low pressure (density). For example, in the case of the 514 nm laser the spectral resolution of the 600 grooves/mm gratings is of 1.99 cm^{-1} per pixel whereas the spectral resolution for the 1800 grooves/mm gratings is almost four times higher at 0.575 cm^{-1} per pixel.

The reproducibility and linearity inconsistencies observed with the single vs. extended or multiwindow methods described above were

Fig. 8. Density of CO_2 as a function of the Fermi diad splitting (Δ) for various instrumental configurations. (A) CO_2 density as a function of the Fermi diad splitting (Δ), all measured using the 532 nm laser but with different gratings. (B) CO_2 density as a function of the Fermi diad splitting (Δ), all measured using the 632 nm laser but different gratings. (C) CO_2 density as a function of the Fermi diad splitting (Δ), all measured using the 514 nm laser but different gratings. In all three cases, the splitting of the Fermi diad for a given density decreases as the resolution of the gratings (more grooves/mm) increases. The data collected with the 600 grooves/mm gratings show greater dispersion due to the lower spectral resolution. (D–F) Fermi diad splitting as a function of density for different laser and gratings combinations, comparing the data before and after correction using the positions of the simultaneously collected Ne lines. Also shown is relationship between Fermi diad splitting and density predicted by Eq. (3) (dashed line).

observed for all of the Raman instruments tested. The distance between the peaks of the Fermi diad at 600 psi and ambient temperature was measured using single window and extended/multiwindow in consecutive collections. For the USGS Raman system (532 nm laser and 1800 gratings) the variation in the splitting of the Fermi diad for different collections was between 0.4 and 0.6 cm^{-1}, and with the XploRA system (532 nm laser and 1800 gratings) the variation in peak splitting was between 0.3 and 0.5 cm^{-1}, similar to what was observed using the Virginia Tech JY Horiba LabRam system.

As noted above, during calibration to develop the densimeters, the pressure corresponding to a given Fermi diad peak splitting is easily measured using a pressure cell and is, therefore, accurately known, and this value is converted to density using an equation of state (EOS).

Here, we consider whether the differences in densimeters could be the result of which EOS was used to interpret the PVT data to convert the measured pressure into the corresponding CO_2 density. Kawakami et al. (2003) and Yamamoto and Kagi (2006) used the Sterner and Pitzer (1994) EOS to calculate the CO_2 density corresponding to the PT conditions at which the Raman spectrum was collected, while the other studies described here used the Span and Wagner (1996) EOS. The differences in density calculated at the same temperature from 0.1 MPa to 200 MPa using Sterner and Pitzer (1994) and Span and Wagner (1996) EOS are <1%, with a standard deviation of 0.43%. This difference is negligible and cannot account for the differences observed between the Kawakami et al. (2003) and Yamamoto and Kagi (2006) data sets and data from other studies described above.
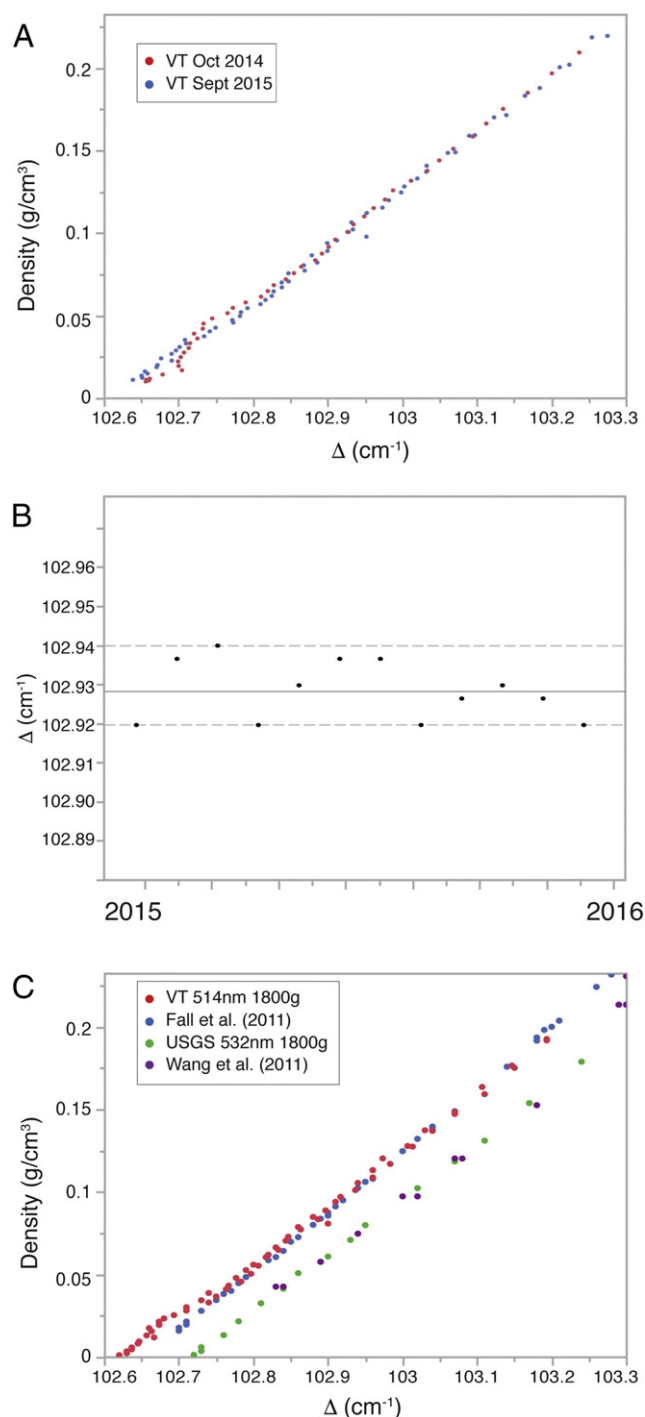
Fig. 9. Comparison of the relationship between Fermi diad peak splitting and density determined at different times. (A) Relationship between Fermi diad splitting (Δ) and density determined in October 2014 and in September 2015 using the 514 nm laser and 1800 groove/mm gratings at Virginia Tech. (B) Measurement of the splitting of the Fermi diad of CO_2 in the HPOC at 500 psi and room temperature at various times over the course of ~1 year. (C) Comparison of the relationship between splitting of the Fermi diad and density obtained in this study (VT 514 nm 1800 g) and data collected at other times using the same Raman configuration, laser wavelength and grating resolution. The data collected in this study and data from Fall et al. (2011) collected approximately 4 years earlier in the same lab using the same Raman system are nearly identical. Similarly, data collected in the USGS lab in this study correlates well with data previously collected by Wang et al. (2011) using the same instrument.

4.3. Temporal variations

The calibration experiments used to develop the densimeter described by eq. (3) were conducted in October 2014. In an effort to understand the long-term reproducibility of the densimeter developed in this study, a second calibration experiment was conducted in September 2015 using the same Raman setup and collection protocols used to determine the densimeter described by Eq. (3). The September 2015 data show almost perfect correlation with the October 2014 data (Fig. 9A). The maximum deviation between the data sets is about 0.02 cm^{-1}, corresponding to a density variation of 0.003 g/cm^{-1}, with a standard deviation of ~0.004 cm^{-1} or 0.001 g/cm^3. The difference in the slopes of the densimeters is 2.8%.

In addition to these two calibrations that were done over the complete range of pressures and densities in the CO_2 vapor field at ambient temperature, the Fermi diad was measured episodically at a fixed pressure, using the same instrumental settings (514 nm laser, and 1800 grooves/mm gratings) and collection protocols used to develop the densimeters. Fig. 9B shows the variations found in the splitting of the Fermi diad at 500 psi (3.5 MPa) and ambient temperature over the course of one year. The average Fermi diad peak splitting for 12 different measurements was 102.93 cm^{-1}, with a maximum deviation of 0.02 cm^{-1} equivalent to an error in density of 0.002 g/cm^3 with a standard deviation of 0.007 cm^{-1} equivalent to an error in density of 0.001 g/cm^3.

We further examined temporal variations in the relationship between Fermi diad peak splitting and density by comparing calibrations conducted on the same Raman instrument and with the same hardware combinations (gratings, laser, etc.), and using the same analytical protocols, but at different times. For example, the relationship between Fermi diad peak splitting and density was determined at Virginia Tech using the JY Horiba LabRam HR800 instrument with 514 nm laser with 1800 grating, and was also determined approximately 4 years earlier by Fall et al. (2011) using the same configuration and instrument (Fig. 9C). As shown, the results for the 2011 calibration (Fall et al., 2011) and those for the more recent calibration (labeled "VT 514 nm 1800 g" in Fig. 9C) are essentially identical. The same consistency for the relationship between Fermi diad peak splitting and density with time is observed between data collected in 2015 as part of this study (labeled "USGS 532 nm 1800 g" in Fig. 9C) using the USGS Raman JY Horiba LabRam HR800 system with 532 nm laser and 1800 gratings and the previously published data from Wang et al. (2011) obtained using the same configuration and instrument (Fig. 9C). These results show that, even though the densimeters determined using the two different instruments and laboratories (VT versus USGS) and collection parameters are noticeably different, the densimeters determined using the same instrument and laboratory and collection parameters are essentially identical, even though they were obtained years apart.

5. Summary and recommendations

We determined the relationship between the splitting of the Fermi diad of CO_2 and CO_2 density at pressures from the liquid-vapor curve (6.0 MPa) to 0.06 MPa at ambient temperature (~22 °C). Twelve experiments were conducted to test the variability associated with instrumental and analytical conditions, as well as to understand the differences between the various densimeters, using three different Raman instruments, with various laser sources and gratings.

All densimeters show a linear and nearly parallel behavior throughout the experimental range of pressures examined here (~0.06 to 6.0 MPa). The slopes of the density versus peak splitting relationship determined here, as well as low density (pressure) data from other published densimeters (Kawakami et al., 2003; Yamamoto and Kagi, 2006; Song et al., 2009; Fall et al., 2011; Wang et al., 2011) (Table 4) are remarkably similar. The differences observed in all densimeters, including previously published densimeters and the 12 experiments from

this study, are most likely a function of variations in instrumentation, laser excitation wavelength, gratings and analytical protocols used during the experimental calibration of the splitting of the Fermi diad.

Based on the results of this examination of the various factors that affect the relationship between Fermi diad splitting and CO_2 pressure, the following protocols are recommended.

1) A densimeter from the literature should not be used to interpret Raman data. A densimeter developed on the Raman instrument used to analyze unknowns, following the calibration procedures used in this study, will be much more reliable. This requires access to samples or equipment that allow the splitting of the Fermi diad to be measured over the complete range of PTX conditions for which the densimeter is to be applied. Fortunately, all of the calibration curves obtained in this study and reported for published densimeters are linear over for density <0.2 g/cm³. Thus, only two samples of known CO_2 density are needed to calibrate the densimeter for any instrument.

2) The linearity of the Raman spectrometer should be determined using positions of known lines (peaks) that bracket or include the spectral region of interest. In this study we used Ne emission lines, but laser lines may also be used.

3) The Raman spectrum should be obtained using a single window collection protocol whereby all peaks of interest are collected simultaneously, including some well-known Raman lines or standard (in our study Ne lines). To develop the densimeter described here, we selected a spectral window such that the CO_2 Fermi diad and the bracketing Ne lines (1031.42 cm^{-1} and 1458.58 cm^{-1}) were within the same window. Following baseline correction, the peaks of the Fermi diad and the Ne lines were fitted using a Gaussian fit to determine the Fermi diad splitting corrected for the non-linearity of the spectrometer in the spectral region of interest.

Supplementary data to this article can be found online at http://dx.doi.org/10.1016/j.chemgeo.2016.12.034.

Acknowledgements

References

Azbej, T., Severs, M.J., Rusk, B.G., Bodnar, R.J., 2007. In situ quantitative analysis of individual H_2O-CO_2 fluid inclusions by laser Raman spectroscopy. Chem. Geol. 237 (3-4), 255–263.

Bakker, R.J., Diamond, L.W., 2000. Determination of the composition and molar volume of H_2O-CO_2 fluid inclusions by microthermometry. Geochim. Cosmochim. Acta 64 (10), 1753–1764.

Bartoli, O., Cesare, B., Poli, S., Bodnar, R.J., Acosta-Vigil, A., Frezzotti, M.L., Meli, S., 2013. Recovering the composition of melt and the fluid regime at the onset of crustal anatexis and S-type granite formation. Geology 41 (2), 115–118.

Bodnar, R.J., 1983. A method of calculating fluid inclusion volumes based on vapor bubble diameters and P-V-T-X properties of inclusion fluids. Econ. Geol. 78, 535–542.

Bodnar, R.J., 1995. Fluid inclusion evidence for a magmatic source for metals in porphyry copper deposits. In: Thompson, J.F.H. (Ed.), Magmas, Fluids and Ore Deposits. Mineral Association of Canada Short Course Vol. 23, pp. 139–152.

Bodnar, R.J., Reynolds, T.J., Kuehn, C.A., 1985. Fluid inclusion systematics in epithermal systems. in, Geology and Geochemistry of Epithermal Systems. In: Berger, B.R., Bethke, P.M. (Eds.), Society of Economic Geologists. Reviews in Econ. Geol Vol. 2, pp. 73–98.

Bodnar, R.J., Lecumberi-Sanches, P., Moncada, D., Steele-MacInnis, M., 2014. Fluid inclusions in hydrothermal ore deposits. Treatise on Geochemistry, second ed., pp. 119–142.

Bottinga, Y., Richet, P., 1981. High pressure and temperature equation of state and calculation of the thermodynamic properties of gaseous carbon dioxide. Am. J. Sci. 281 (5), 615–660.

Charlou, J.L., Fouquet, Y., Bougault, H., Donval, J.P., Etoubleau, J., Jean-Baptiste, P., Rona, P.A., 1998. Intense CH_4 plumes generated by serpentinization of ultramafic rocks at the intersection of the 15° 20′ N fracture zone and the Mid-Atlantic Ridge. Geochim. Cosmochim. Acta 62 (13), 2323–2333.

Charlou, J.L., Donval, J.P., Fouquet, Y., Jean-Baptiste, P., Holm, N., 2002. Geochemistry of high H_2 and CH_4 vent fluids issuing from ultramafic rocks at the Rainbow hydrothermal field (36° 14′ N, MAR). Chem. Geol. 191 (4), 345–359.

Chiodini, G., Cioni, R., Guidi, M., Raco, B., Marini, L., 1998. Soil CO_2 flux measurements in volcanic and geothermal areas. Appl. Geochem. 13 (5), 543–552.

Di Genova, D., Romano, C., Alletti, M., Misiti, V., Scarlato, P., 2014. The effect of CO_2 and H_2O on Etna and Fondo Riccio (Phlegrean Fields) liquid viscosity, glass transition temperature and heat capacity. Chem. Geol. 377, 72–86.

Duschek, W., Kleinrahm, R., Wagner, W., 1990. Measurement and correlation of the (pressure, density, temperature) relation of carbon dioxide I. The homogeneous gas and liquid regions in the temperature range from 217 K to 340 K at pressures up to 9 MPa. J. Chem. Thermodyn. 22 (9), 827–840.

Esposito, R., Bodnar, R.J., Danyushevsky, L.V., De Vivo, B., Fedele, L., Hunter, J., Shimizu, N., 2011. Volatile evolution of magma associated with the Sochiaro eruption in the Phlegrean Volcanic District (Italy). J. Petrol. 52, 2431–2460.

Esposito, R., Lamadrid, H.M., Redi, D., Steele-MacInnis, M., Bodnar, R.J., Manning, C.E., De Vivo, B., Cannatelli, C., Lima, A., 2016. Detection of liquid H_2O in vapor bubbles in melt inclusions: implications for magmatic fluid composition and volatile budgets of magmas? Am. Mineral. 101, 1691–1695.

Fall, A., Tattitch, B., Bodnar, R.J., 2011. Combined microthermometric and Raman spectroscopic technique to determine the salinity of H_2O-CO_2-NaCl fluid inclusions based on clathrate melting. Geochim. Cosmochim. Acta 75, 951–964.

Fermi, E., 1931. Über den Ramaneffekt des kolendioxyds. Z. Phys. 71, 250–259.

Frezzotti, M.L., Ferrando, S., 2015. The chemical behavior of fluids released during deep subduction based on fluid inclusions. Am. Mineral. 100 (2-3), 352–377.

Frezzotti, M.L., Touret, J.L., Lustenhouwer, W.J., Neumann, E.R., 1994. Melt and fluid inclusions in dunite xenoliths from La Gomera, Canary Islands: tracking the mantle metasomatic fluids. Eur. J. Mineral. 805–818.

Fukura, S., Mizukami, T., Odake, S., Kagi, H., 2006. Factors determining the stability, resolution, and precision of a conventional Raman spectrometer. Appl. Spectrosc. 60, 946–950.

Gaufrès, R., Huguet, P., Arab, Y., 1995. Method for the determination of spectral shifts in Raman spectroscopy. J. Raman Spectrosc. 26 (3), 243–253.

Giggenbach, W.F., 1988. Geothermal solute equilibria. Derivation of Na-K-Mg-Ca geoindicators. Geochim. Cosmochim. Acta 52 (12), 2749–2765.

Giggenbach, W.F., 1996. Chemical composition of volcanic gases. Monitoring and Mitigation of Volcano Hazards. Springer, Berlin Heidelberg, pp. 221–256.

Gordon, H.R., McCubbin, T.K., 1966. The 2.8-micron bands of CO_2. J. Mol. Spectrosc. 19, 137–154.

Hartley, M.E., Maclennan, J., Edmonds, M., Thordarson, T., 2014. Reconstructing the deep CO_2 degassing behavior of large basaltic fissure eruptions. Earth Planet. Sci. Lett. 393, 120–121.

Hedenquist, J.W., Henley, R.W., 1985. The importance of CO_2 on freezing point measurements of fluid inclusions; evidence from active geothermal systems and implications for epithermal ore deposition. Econ. Geol. 80 (5), 1379–1406.

Hollister, L.S., Burruss, R.C., 1976. Phase equilibria in fluid inclusions from the Khtada Lake metamorphic complex. Geochim. Cosmochim. Acta 40 (2), 163–175.

Izraeli, E.S., Harris, J.W., Navon, O., 1999. Raman barometry of diamond formation. Earth Planet. Sci. Lett. 173, 351–360.

Kawakami, Y., Yamamoto, J., Kagi, H., 2003. Micro-Raman densimeter for the CO_2 inclusions in mantle-derived minerals. Appl. Spectrosc. 57, 1333–1339.

Kelley, D.S., 1996. Methane-rich fluids in the oceanic crust. J. Geophys. Res. Solid Earth 101 (B2), 2943–2962.

Kent, A.J., 2008. Melt inclusions in basaltic and related volcanic rocks. Rev. Mineral. Geochem. 69 (1), 273–331.

Lin, F., Bodnar, R.J., Becker, S.P., 2007. Experimental determination of the Raman CH_4 symmetric stretching (ν_1) band position from 1–650 bar and 0.3–22 °C: application to fluid inclusion studies. Geochim. Cosmochim. Acta 71, 3746–3756.

Lowenstern, J.B., 2001. Carbon dioxide in magmas and implications for hydrothermal systems. Miner Depos 36 (6), 490–502.

Lu, W., Chou, I.M., Burruss, R.C., Song, Y., 2007. A unified equation for calculating methane vapor pressures in the CH_4 – H_2O system with measured Raman shifts. Geochim. Cosmochim. Acta 71 (16), 3969–3978.

McCreery, R.L., 2000. Raman Spectroscopy for Chemical Analysis. John Wiley and Sons (448 pp.).

Mestari, A., Gaufrès, R., Huguet, P., 1997. Behaviour of the calibration of a Raman spectrometer with temperature changes. J. Raman Spectrosc. 28 (10), 785–789.

Métrich, N., Wallace, P.J., 2008. Volatile abundances in basaltic magmas and their degassing paths tracked by melt inclusions. Rev. Mineral. Geochem. 69 (1), 363–402.

Moore, L.R., Gazel, E., Tuohy, R., Lloyd, A., Esposito, R., Steele-MacInnis, M., Hauri, E.H., Wallace, P.J., Plank, T., Bodnar, R.J., 2015. Bubbles matter: an assessment of the contribution of vapor bubbles to melt inclusion volatile budgets. Am. Mineral. 100 (4), 806–823.

Mormone, A., Piochi, M., Bellatreccia, F., De Astis, G., Moretti, R., Della Ventura, G., Carballo, A., Mangiacapra, A., 2011. A CO_2-rich magma source beneath the Phlegraean Volcanic

District (Southern Italy): Evidence from a melt inclusion study. Chem. Geol. 287 (1), 66–80.

Newton, R.C., Smith, J.V., Windley, B.F., 1980. Carbonic metamorphism, granulites and crustal growth. Nature 288, 45–50.

Roedder, E., 1965. Liquid CO_2 inclusions in olivine-bearing nodules and phenocrysts from basalts. Am. Mineral. 50, 1746–1782.

Roedder, E., 1984. Fluid inclusions, Mineralogy Society of America. Rev. Mineral. 12 (644 pp.).

Roedder, E., 1994. Fluid inclusion evidence of mantle fluids. In: De Vivo, B., Frezzotti, M.L. (Eds.), Fluid Inclusions in Minerals: Methods and Applications. Virginia Polytechnic Institute and State University, Blacksburg, pp. 283–296.

Roedder, E., Bodnar, R.J., 1997. Fluid inclusion studies of hydrothermal ore deposits. In: Barnes, H.L. (Ed.), Geochemistry of Hydrothermal Ore Deposits, third ed. Wiley and Sons Inc., New York, pp. 657–698.

Rosso, K.M., Bodnar, R.J., 1995. Detection limits of CO_2 in fluid inclusions using microthermometry and laser Raman spectroscopy and the spectroscopic characterization of CO_2. Geochim. Cosmochim. Acta 59, 3961–3975.

Song, Y., Chou, I.M., Hu, W., Burruss, R., Lu, W., 2009. CO_2 density-Raman shift relation derived from synthetic inclusions in fused capillaries and its application. Acta Geol. Sin. 83, 932–938.

Span, R., Wagner, W., 1996. A new equation of state for carbon dioxide covering the fluid region from the triple point temperature to 1100 K at pressures up to 800 MPa. J. Phys. Chem. 25, 1509–1596.

Steele-MacInnis, M., Esposito, R., Bodnar, R.J., 2011. Thermodynamic model for the effect of post-entrapment crystallization on the H_2O-CO_2 systematics of vapor-saturated, silicate melt inclusions. J. Petrol. 52, 2461–2482.

Sterner, S.M., Pitzer, K.S., 1994. An equation of state for carbon dioxide valid from zero to extreme pressures. Contrib. Mineral. Petrol. 117 (4), 362–374.

Touret, J., 1971. Le facies granulite en Norvege Meridionale: II. Les inclusions fluides. Lithos 4 (4), 423–436.

Touret, J., 1981. Fluid inclusions in high-grade metamorphic rocks. In: Hollister, L.S., Crawford, M.L. (Eds.), Fluid Inclusions: Applications to Petrology. Mineralogy Association of Canada, Short Course Vol. 6, pp. 182–208.

Touret, J., 2001. Fluids in metamorphic rocks. Lithos 55, 1–25.

Wallace, P.J., 2005. Volatiles in subduction zone magmas: concentrations and fluxes based on melt inclusion and volcanic gas data. J. Volcanol. Geotherm. Res. 140, 217–240.

Wang, X., Chou, I.M., Hu, W., Burruss, R.C., Sun, Q., Song, Y., 2011. Raman spectroscopic measurements of CO_2 density: experimental calibration with high-pressure optical cell (HPOC) and fused silica capillary capsule (FSCC) with application to fluid inclusion observations. Geochim. Cosmochim. Acta 75 (14), 4080–4093.

Wright, R.B., Wang, C.H., 1973. Density effect on the Fermi resonance in gaseous CO_2 Raman scattering. J. Chem. Phys. 58, 2893–2895.

Wright, R.B., Wang, C.H., 1975. Effect of density on the Raman scattering of molecular fluids. II. Study of intermolecular interactions in CO_2. J. Chem. Phys. 61, 2707–2710.

Yamamoto, J., Kagi, H., 2006. Extended micro-Raman densimeter for CO_2 applicable to mantle-originated fluid inclusions. Chem. Lett. 35, 610–611.

Yamamoto, J., Kagi, H., Kaneoka, I., Lai, Y., Prikhod'ko, V.S., Arai, S., 2002. Fossil pressures of fluid inclusions in mantle xenoliths exhibiting rheology of mantle minerals: implications for the geobarometry of mantle minerals using micro-Raman spectroscopy. Earth Planet. Sci. Lett. 198 (3), 511–519.

Yamamoto, J., Kagi, H., Kawakami, Y., Hirano, N., Nakamura, M., 2007. Paleo-Moho depth determined from the pressure of CO_2 fluid inclusions: Raman spectroscopic barometry of mantle-and crust-derived rocks. Earth Planet. Sci. Lett. 253 (3), 369–377.

Yardley, B.W.D., 1997. The evolution of fluids through the metamorphic cycle. In: Jamtveit, B., Yardley, B.W.D. (Eds.), Fluid Flow and Transport in Rocks. Springer, pp. 99–121.

Yardley, B.W.D., Bodnar, R.J., 2014. Fluids in the continental crust. Geochem. Perspect. 3 (1), 1–12.